Magnetic Properties of the Ferrimagnetic Blume-Capel Model with Mixed Spin- $\frac{5}{2}$ and Spin-3: Exact Recursion Relations Approach

M. Kake^a, T.D. Oke^{a,b}, R.A.A. Yessoufou^{a,b}, R. Houenou^a, E. Albayrak^{c,*} and A. Kpadonou^{a,d}

Received: 05.11.2025 & Accepted: 24.04.2025

Doi: 10.12693/APhysPolA.147.435

*e-mail: albayrak@erciyes.edu.tr

We employ the exact recursion relations to investigate the magnetic properties of a ferrimagnetic Blume–Capel model composed of mixed spins 5/2 and 3 on the Bethe lattice, considering only nearest-neighbor interactions. The ground state phase diagrams are constructed in the $(D_A/q|J|,D_B/q|J|)$ plane, revealing multiple possible ground states, multiphase points, and phase boundaries. Temperature-dependent phase diagrams are systematically derived for various single-ion anisotropies, demonstrating a wide range of critical phenomena, including first- and second-order phase transitions, tricritical points, compensation temperatures, and reentrant behavior in the absence of a magnetic field. Notably, the system exhibits up to four distinct compensation temperatures depending on the values of the crystal field parameters. Additionally, under an applied magnetic field, the system exhibits complex hysteresis behaviors, including single, double, and triple hysteresis loops, which emerge for specific parameter regimes. These findings underscore the intricate interplay between anisotropy, thermal fluctuations, and external field in governing the magnetic response of mixed-spin ferrimagnetic systems.

topics: recursion relations, Blume–Capel Ising ferrimagnetic model, Bethe lattice, compensation temperature

1. Introduction

The study of mixed-spin Ising models [1, 2] has garnered significant research interest due to their richer physical properties compared to single-spin systems. In particular, mixed-spin ferrimagnetic Ising models [3–6] have been widely investigated as they provide a powerful framework for understanding ferrimagnetism in insulating materials, which is essential for both fundamental research and technological applications [7–11].

Extensive theoretical studies [12–17] have explored binary systems of the form A_pB_{1-p} combining half-integer spins (e.g., 1/2, 3/2, 5/2, 7/2) with integer spins (e.g., 1, 2, 3). The growing focus on systems containing at least one spin greater than 3/2 stems from their ability

to reveal novel magnetic phenomena. These systems have been analyzed using various approaches, including Monte Carlo simulations [1, 3, 18–21], mean-field theory [5, 6, 22–24], and exact recursion relations [25–34]. It has been established that crystal field effects on spin sites can significantly modify magnetic behavior, influencing phase transitions and critical phenomena such as compensation, hysteresis, tricriticality, and reentrant behavior, which are also strongly dependent on lattice geometry.

The mixed-spin $(\frac{5}{2},3)$ configuration naturally emerges in several magnetic oxides, where transition metal ions adopt these spin states due to their electronic structures. A notable example is cobalt ferrite (CoFe₂O₄), where Fe³⁺ $(s=\frac{5}{2})$ and Co²⁺ (s=3) interact within a ferrimagnetic spinel structure, imparting strong magnetic anisotropy and high coercivity — key properties for spintronic

^aInstitute of Mathematics and Physical Sciences (IMSP), University of Abomey-Calavi, BP: 613, 229, Dangbo, Benin

^bFaculty of Sciences and Techniques (FAST), University of Abomey-Calavi, BP: 526, 229, Abomey-Calavi, Benin

^cErciyes University, Department of Physics, Köşk Mah. Kutadgu Bilig Sk. 38030, Melikgazi, Kayseri, Turkey

^dENS and Laboratory of Physics and Applications, UNSTIM of Abomey, BP: 486, 229, Abomey, Benin

applications [35]. Additionally, perovskite oxides such as LaMn_{0.5}Fe_{0.5}O₃ and NdMn_{0.5}Fe_{0.5}O₃ exhibit similar spin combinations, where Fe³⁺ ($s=\frac{5}{2}$) and Mn³⁺ (s=3) modulate ferrimagnetic or antiferromagnetic behavior depending on temperature and chemical composition [36]. These materials serve as relevant experimental platforms for testing theoretical mixed-spin ($\frac{5}{2}$, 3) models, validating predictions related to magnetic ordering, compensation phenomena, and phase transitions.

Despite their relevance, only a few recent studies employing mean-field theory have specifically examined the ferrimagnetic Ising model for the mixed spin-5/2 and spin-3 [37, 38]. These investigations, focused on the Blume-Capel model, identified multiple compensation points in a disordered system for square and simple cubic lattices, as well as reentrant phase transitions between ordered phases. However, to our knowledge, the model has only been explored within the mean-field theory. Furthermore, studies on related models have predicted the existence of tricritical points and multi-hysteresis behavior [18, 19], features yet to be documented for this specific system.

This work advances previous works [37, 38] by analyzing the effects of two distinct anisotropies on the phase diagrams and compensation temperatures of a mixed-spin (5/2,3) Ising ferrimagnetic system, employing the exact recursion relations method [25–34].

The remainder of this paper is structured as follows: Sect. 2 presents the model and methodological framework, Sect. 3 discusses the main numerical results, and Sect. 4 provides the conclusions.

2. Model and method description

We consider the Blume–Capel model of a mixed spin-5/2 and spin-3 Ising ferrimagnetic system defined on the Bethe lattice, as illustrated in Fig. 1. Its Hamiltonian is given by

$$H = -J \sum_{\langle i,j \rangle} s_i \sigma_j - D_A \sum_i s_i^2 - D_B \sum_j \sigma_j^2$$
$$-h \Big(\sum_i s_i + \sum_j \sigma_j \Big). \tag{1}$$

Spin-5/2 can take eigenvalues $s_i = \pm 5/2$, $\pm 3/2$, $\pm 1/2$, while spin-3 can take $\sigma_j = \pm 3, \pm 2, \pm 1, 0$. In (1), D_A and D_B represent the crystal field effects on spin-5/2 and spin-3 sites, respectively, h denotes the external magnetic field, and J characterizes the antiferromagnetic interactions between s_i and σ_j .

The Bethe lattice is structured with a central spin-5/2, followed by alternating generations of spin-3 and spin-5/2 sites extending indefinitely, as shown in Fig. 1. The choice of the central spin, whether spin-5/2 or spin-3, has no impact on the system's physical properties.

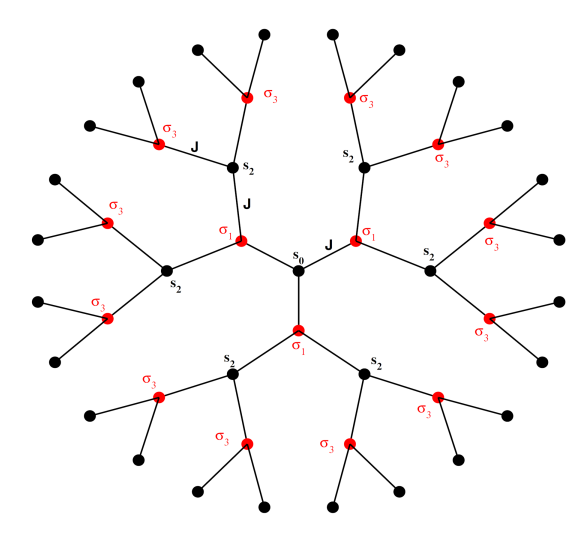


Fig. 1. Schematic representation of the Bethe lattice with coordination number q=3, consisting of two interpenetrating sublattices with spins s=5/2 and $\sigma=3$. Black circles represent spin-5/2 particles, while red circles correspond to spin-3 particles.

In order to obtain the exact recursion relation on the Bethe lattice, some detailed calculations are necessary. However, we direct readers to the previous works for all the details [25–34] and give only the final results. Given that $\sigma_1=\pm 3,\pm 2,\pm 1,0$, the partial partition function of the central spin s_0 can be calculated as follows

$$g_{n}(s_{0}) = \sum_{\sigma_{1}} \exp\left[\beta\left(Js_{0}\sigma_{1} + D_{B}\sigma_{1}^{2} + h\sigma_{1}\right)\right] g_{m}^{p}(\sigma_{1}) =$$

$$e^{\beta(3Js_{0} + 9D_{B} + 3h)} g_{m}^{p}(+3)$$

$$+ e^{\beta(3Js_{0} + 9D_{B} - 3h)} g_{m}^{p}(-3)$$

$$+ e^{\beta(2Js_{0} + 4D_{B} + 2h)} g_{m}^{p}(+2)$$

$$+ e^{\beta(-2Js_{0} + 4D_{B} - 2h)} g_{m}^{p}(-2)$$

$$+ e^{\beta(Js_{0} + D_{B} + h)} g_{m}^{p}(+1)$$

$$+ e^{\beta(-Js_{0} + D_{B} - h)} g_{m}^{p}(-1) + g_{m}^{p}(0), \tag{2}$$

where p = q - 1 and m = n - 1. Since the central spin s_0 can take six eigenvalues $(\pm 5/2, \pm 3/2, \pm 1/2)$, the system has six corresponding partial partition functions, given by

$$g_{n}\left(\pm\frac{5}{2}\right) = e^{\beta(\pm15J/2+9D_{B}+3h)}g_{m}^{p}(+3)$$

$$+ e^{\beta(\mp15J/2+9D_{B}-3h)}g_{m}^{p}(-3)$$

$$+ e^{\beta(\pm5J+4D_{B}+2h)}g_{m}^{p}(+2)$$

$$+ e^{\beta(\mp5J+4D_{B}-2h)}g_{m}^{p}(-2)$$

$$+ e^{\beta(\pm5J/2+D_{B}+h)}g_{m}^{p}(+1)$$

$$+ e^{\beta(\mp5J/2+D_{B}-h)}g_{m}^{p}(-1) + g_{m}^{p}(0), \tag{3}$$

$$g_{n}\left(\pm\frac{3}{2}\right) = e^{\beta(\pm9J/2+9D_{B}+3h)}g_{m}^{p}(+3)$$

$$+ e^{\beta(\mp9J/2+9D_{B}-3h)}g_{m}^{p}(-3)$$

$$+ e^{\beta(\pm3J+4D_{B}+2h)}g_{m}^{p}(+2)$$

$$+ e^{\beta(\mp3J+4D_{B}-2h)}g_{m}^{p}(-2)$$

$$+ e^{\beta(\pm3J/2+D_{B}+h)}g_{m}^{p}(+1)$$

$$+ e^{\beta(\mp3J/2+D_{B}-h)}g_{m}^{p}(-1) + g_{m}^{p}(0), \tag{4}$$

and

$$g_{n}\left(\pm\frac{1}{2}\right) = e^{\beta(\pm3J/2+9D_{B}+3h)}g_{m}^{p}(+3)$$

$$+ e^{\beta(\mp3J/2+9D_{B}-3h)}g_{m}^{p}(-3)$$

$$+ e^{\beta(\pm J+4D_{B}+2h)}g_{m}^{p}(+2)$$

$$+ e^{\beta(\mp J+4D_{B}-2h)}g_{m}^{p}(-2)$$

$$+ e^{\beta(\pm J/2+D_{B}+h)}g_{m}^{p}(+1)$$

$$+ e^{\beta(\mp J/2+D_{B}-h)}g_{m}^{p}(-1) + g_{m}^{p}(0).$$
 (5)

In order to identify the recursion relations, we take any of the partial partition functions and take the ratio with the rest, chosen to be $g_n(-1/2)$. Thus the recursion relations for spin-5/2 are given as

$$X_{1} = \frac{g_{n}(+\frac{5}{2})}{g_{n}(-\frac{1}{2})} = \frac{1}{X_{0}} \left[e^{\beta(15J/2 + 9D_{B} + 3h)} Y_{1}^{p} + e^{\beta(-15J/2 + 9D_{B} - 3h)} Y_{2}^{p} + e^{\beta(5J + 4D_{B} + 2h)} Y_{3}^{p} + e^{\beta(-5J + 4D_{B} - 2h)} Y_{4}^{p} + e^{\beta(5J/2 + D_{B} + h)} Y_{5}^{p} + e^{\beta(-5J/2 + D_{B} - h)} Y_{6}^{p} + 1 \right],$$

$$(6)$$

$$X_{2} = \frac{g_{n}(-\frac{5}{2})}{g_{n}(-\frac{1}{2})} = \frac{1}{X_{0}} \left[e^{\beta(-15J/2 + 9D_{B} + 3h)} Y_{1}^{p} + e^{\beta(15J/2 + 9D_{B} - 3h)} Y_{2}^{p} + e^{\beta(-5J + 4D_{B} + 2h)} Y_{3}^{p} + e^{\beta(5J + 4D_{B} - 2h)} Y_{4}^{p} + e^{\beta(-5J/2 + D_{B} + h)} Y_{5}^{p} + e^{\beta(5J/2 + D_{B} - h)} Y_{6}^{p} + 1 \right],$$

$$(7)$$

$$X_{3} = \frac{g_{n}(+\frac{3}{2})}{g_{n}(-\frac{1}{2})} = \frac{1}{X_{0}} \left[e^{\beta(9J/2+9D_{B}+3h)} Y_{1}^{p} + e^{\beta(-9J/2+9D_{B}-3h)} Y_{2}^{p} + e^{\beta(3J+4D_{B}+2h)} Y_{3}^{p} + e^{\beta(-3J+4D_{B}-2h)} Y_{4}^{p} + e^{\beta(3J/2+D_{B}+h)} Y_{5}^{p} + e^{\beta(-3J/2+D_{B}-h)} Y_{6}^{p} + 1 \right],$$
(8)

$$X_{4} = \frac{g_{n}(-\frac{3}{2})}{g_{n}(-\frac{1}{2})} = \frac{1}{X_{0}} \left[e^{\beta(-9J/2+9D_{B}+3h)} Y_{1}^{p} + e^{\beta(9J/2+9D_{B}-3h)} Y_{2}^{p} + e^{\beta(-3J+4D_{B}+2h)} Y_{3}^{p} + e^{\beta(3J+4D_{B}-2h)} Y_{4}^{p} + e^{\beta(-3J/2+D_{B}+h)} Y_{5}^{p} + e^{\beta(3J/2+D_{B}-h)} Y_{6}^{p} + 1 \right],$$

$$(9)$$

$$X_{5} = \frac{g_{n}(+\frac{1}{2})}{g_{n}(-\frac{1}{2})} = \frac{1}{X_{0}} \left[e^{\beta(3J/2+9D_{B}+3h)} Y_{1}^{p} + e^{\beta(-3J/2+9D_{B}-3h)} Y_{2}^{p} + e^{\beta(J+4D_{B}+2h)} Y_{3}^{p} + e^{\beta(-J+4D_{B}-2h)} Y_{4}^{p} + e^{\beta(J/2+D_{B}+h)} Y_{5}^{p} + e^{\beta(-J/2+D_{B}-h)} Y_{6}^{p} + 1 \right],$$

$$(10)$$

where

$$X_{0} = e^{\beta(-3J/2+9D_{B}+3h)}Y_{1}^{p} + e^{\beta(3J/2+9D_{B}-3h)}Y_{2}^{p}$$

$$+ e^{\beta(-J+4D_{B}+2h)}Y_{3}^{p} + e^{\beta(J+4D_{B}-2h)}Y_{4}^{p}$$

$$+ e^{\beta(-J/2+D_{B}+h)}Y_{5}^{p} + e^{\beta(J/2+D_{B}-h)}Y_{6}^{p} + 1.$$
(11)

Similarly, we need the recursion relations for the spin-3, whose partial partition function is defined as follows

$$g_{m}(\sigma_{1}) = \sum_{s_{2}} \exp\left[\beta\left(Js_{2}\sigma_{1} + D_{A}s_{2}^{2} + hs_{2}\right)\right] g_{r}^{p}(s_{2}) =$$

$$e^{\frac{\beta}{2}(5J\sigma_{1} + 25D_{A}/2 + 5h)} g_{r}^{p}\left(+\frac{5}{2}\right)$$

$$+ e^{\frac{\beta}{2}(-5J\sigma_{1} + 25D_{A}/2 - 5h)} g_{r}^{p}\left(-\frac{5}{2}\right)$$

$$+ e^{\frac{\beta}{2}(3J\sigma_{1} + 9D_{A}/2 + 3h)} g_{r}^{p}\left(+\frac{3}{2}\right)$$

$$+ e^{\frac{\beta}{2}(-3J\sigma_{1} + 9D_{A}/2 - 3h)} g_{r}^{p}\left(-\frac{3}{2}\right)$$

$$+ e^{\frac{\beta}{2}(J\sigma_{1} + D_{A}/2 + h)} g_{r}^{p}\left(+\frac{1}{2}\right)$$

$$+ e^{\frac{\beta}{2}(-J\sigma_{1} + D_{A}/2 - h)} g_{r}^{p}\left(-\frac{1}{2}\right). \tag{12}$$

By applying (12) to the given eigenvalues of s and σ , we obtain

$$g_{m}(\pm 3) = e^{\frac{\beta}{2}(\pm 15J + 25D_{A}/2 + 5h)}g_{r}^{p}\left(\pm \frac{5}{2}\right)$$

$$+ e^{\frac{\beta}{2}(\mp 15J + 25D_{A}/2 - 5h)}g_{r}^{p}\left(-\frac{5}{2}\right)$$

$$+ e^{\frac{\beta}{2}(\pm 9J + 9D_{A}/2 + 3h)}g_{r}^{p}\left(\pm \frac{3}{2}\right)$$

$$+ e^{\frac{\beta}{2}(\mp 9J + 9D_{A}/2 - 3h)}g_{r}^{p}\left(-\frac{3}{2}\right)$$

$$+ e^{\frac{\beta}{2}(\pm 3J + D_{A}/2 + h)}g_{r}^{p}\left(\pm \frac{1}{2}\right)$$

$$+ e^{\frac{\beta}{2}(\mp 3J + D_{A}/2 - h)}g_{r}^{p}\left(-\frac{1}{2}\right),$$

$$g_{m}(\pm 2) = e^{\beta(\pm 5J + 25D_{A}/4 + 5h/2)}g_{r}^{p}\left(\pm \frac{5}{2}\right)$$

$$+ e^{\beta(\mp 5J + 25D_{A}/4 - 5h/2)}g_{r}^{p}\left(\pm \frac{5}{2}\right)$$

$$+ e^{\beta(\mp 5J + 25D_{A}/4 - 5h/2)}g_{r}^{p}\left(\pm \frac{5}{2}\right)$$

$$+ e^{\beta(\mp 5J + 25D_A/4 - 5h/2)} g_r^p \left(-\frac{5}{2}\right)$$

$$+ e^{\beta(\pm 3J + 9D_A/4 + 3h/2)} g_r^p \left(+\frac{3}{2}\right)$$

$$+ e^{\beta(\mp 3J + 9D_A/4 - 3h/2)} g_r^p \left(-\frac{3}{2}\right)$$

$$+ e^{\beta(\pm J + D_A/4 + h/2)} g_r^p \left(+\frac{1}{2}\right)$$

$$+ e^{\beta(\mp J + D_A/4 - h/2)} g_r^p \left(-\frac{1}{2}\right), \tag{14}$$

$$g_{m}(\pm 1) = e^{\frac{\beta}{2}(\pm 5J + 25D_{A}/2 + 5h)} g_{r}^{p} \left(+ \frac{5}{2} \right)$$

$$+ e^{\frac{\beta}{2}(\mp 5J + 25D_{A}/2 - 5h)} g_{r}^{p} \left(- \frac{5}{2} \right)$$

$$+ e^{\frac{\beta}{2}(\pm 3J + 9D_{A}/2 + 3h)} g_{r}^{p} \left(+ \frac{3}{2} \right)$$

$$+ e^{\frac{\beta}{2}(\mp 3J + 9D_{A}/2 - 3h)} g_{r}^{p} \left(- \frac{3}{2} \right)$$

$$+ e^{\frac{\beta}{2}(\pm J + D_{A}/2 - h)} g_{r}^{p} \left(+ \frac{1}{2} \right)$$

$$+ e^{\frac{\beta}{2}(\mp J + D_{A}/2 - h)} g_{r}^{p} \left(- \frac{1}{2} \right), \tag{15}$$

$$g_{m}(0) = e^{\frac{\beta}{2}(25D_{A}/2 + 5h)} g_{r}^{p} \left(+ \frac{5}{2} \right)$$

$$+ e^{\frac{\beta}{2}(9D_{A}/2 - 5h)} g_{r}^{p} \left(+ \frac{3}{2} \right)$$

$$+ e^{\frac{\beta}{2}(9D_{A}/2 - 3h)} g_{r}^{p} \left(- \frac{3}{2} \right)$$

$$+ e^{\frac{\beta}{2}(D_{A}/2 + h)} g_{r}^{p} \left(+ \frac{1}{2} \right)$$

$$+ e^{\frac{\beta}{2}(D_{A}/2 - h)} g_{r}^{p} \left(- \frac{1}{2} \right), \tag{16}$$

where r = n - 2. Thus, the recursion relations are given by scaling the partial partition functions by $g_m(0)$, we get

$$\begin{split} g_{m}(0), & \text{we get} \\ Y_{1} &= \frac{g_{m}(+3)}{g_{m}(0)} = \frac{1}{Y_{0}} \Big[e^{\frac{\beta}{2}(15J+25D_{A}/2+5h)} X_{1}^{p} \\ &+ e^{\frac{\beta}{2}(-15J+25D_{A}/2-5h)} X_{2}^{p} + e^{\frac{\beta}{2}(9J+9D_{A}/2+3h)} X_{3}^{p} \\ &+ e^{\frac{\beta}{2}(-9J+9D_{A}/2-3h)} X_{4}^{p} + e^{\frac{\beta}{2}(3J+D_{A}/2+h)} X_{5}^{p} \\ &+ e^{\frac{\beta}{2}(-3J+D_{A}/2-h)} \Big], \end{split} \tag{17}$$

$$Y_{2} &= \frac{g_{m}(-3)}{g_{m}(0)} = \frac{1}{Y_{0}} \Big[e^{\frac{\beta}{2}(-15J+25D_{A}/2+5h)} X_{1}^{p} \\ &+ e^{\frac{\beta}{2}(15J+25D_{A}/2-5h)} X_{2}^{p} + e^{\frac{\beta}{2}(-9J+9D_{A}/2+3h)} X_{3}^{p} \\ &+ e^{\frac{\beta}{2}(9J+9D_{A}/2-3h)} X_{4}^{p} + e^{\frac{\beta}{2}(-3J+D_{A}/2+h)} X_{5}^{p} \\ &+ e^{\frac{\beta}{2}(3J+D_{A}/2-h)} \Big], \end{split} \tag{18}$$

$$Y_{3} &= \frac{g_{m}(+2)}{g_{m}(0)} = \frac{1}{Y_{0}} \Big[e^{\beta(5J+25D_{A}/4+5h/2)} X_{1}^{p} \\ &+ e^{\beta(-5J+25D_{A}/4-5h/2)} X_{2}^{p} + e^{\beta(3J+9D_{A}/4+3h/2)} X_{3}^{p} \\ &+ e^{\beta(-J+D_{A}/4-h/2)} \Big], \end{split} \tag{19}$$

$$Y_{4} &= \frac{g_{m}(-2)}{g_{m}(0)} = \frac{1}{Y_{0}} \Big[e^{\beta(-5J+25D_{A}/4+5h/2)} X_{1}^{p} \\ &+ e^{\beta(5J+25D_{A}/4-5h/2)} X_{2}^{p} + e^{\beta(-3J+9D_{A}/4+3h/2)} X_{3}^{p} \\ &+ e^{\beta(3J+9D_{A}/4-3h/2)} X_{4}^{p} + e^{\beta(-J+D_{A}/4+h/2)} X_{5}^{p} \\ &+ e^{\beta(3J+9D_{A}/4-3h/2)} X_{4}^{p} + e^{\beta(-J+D_{A}/4+h/2)} X_{5}^{p} \end{aligned}$$

 $+ e^{\beta(J+D_A/4-h/2)} \Big],$

$$Y_{5} = \frac{g_{m}(+1)}{g_{m}(0)} = \frac{1}{Y_{0}} \left[e^{\frac{\beta}{2}(5J+25D_{A}/2+5h)} X_{1}^{p} + e^{\frac{\beta}{2}(-5J+25D_{A}/2-5h)} X_{2}^{p} + e^{\frac{\beta}{2}(3J+9D_{A}/2+3h)} X_{3}^{p} + e^{\frac{\beta}{2}(-3J+9D_{A}/2-3h)} X_{4}^{p} + e^{\frac{\beta}{2}(J+D_{A}/2+h)} X_{5}^{p} + e^{\frac{\beta}{2}(-J+D_{A}/2-h)} \right],$$

$$(21)$$

$$Y_{6} = \frac{g_{m}(-1)}{g_{m}(0)} = \frac{1}{Y_{0}} \left[e^{\frac{\beta}{2}(-5J+25D_{A}/2+5h)} X_{1}^{p} + e^{\frac{\beta}{2}(5J/+25D_{A}/2-5h)} X_{2}^{p} + e^{\frac{\beta}{2}(-3J+9D_{A}/2+3h)} X_{3}^{p} + e^{\frac{\beta}{2}(3J+9D_{A}/2-3h)} X_{4}^{p} + e^{\frac{\beta}{2}(-J+D_{A}/2+h)} X_{5}^{p} + e^{\frac{\beta}{2}(J+D_{A}/2-h)} \right],$$

$$(22)$$

whor

$$Y_{0} = e^{\beta(25D_{A}/4+5h/2)}X_{1}^{p} + e^{\beta(25D_{A}/4-5h/2)}X_{2}^{p}$$

$$+ e^{\beta(9D_{A}/4+3h/2)}X_{3}^{p} + e^{\beta(9D_{A}/4-3h/2)}X_{4}^{p}$$

$$+ e^{\beta(D_{A}/4+h/2)}X_{5}^{p} + e^{\beta(D_{A}/4-h/2)}.$$
(23)

After having calculated the recursion relations for spin-5/2 and spin-3, we are now ready to obtain the magnetization values by using them. The magnetization for the spin-5/2 atoms can be obtained from

$$M_{5/2} = Z_{5/2}^{-1} \sum_{\{s_0\}} s_0 P(\{s_0\}) =$$

$$Z_{5/2}^{-1} \sum_{\{s_0\}} s_0 e^{\beta(D_A s_0^2 + h s_0)} g_n^q(s_0), \tag{24}$$

where

$$Z_{5/2} = \sum_{\{s_0\}} e^{\beta(D_A s_0^2 + hs_0)} g_n^q(s_0)$$
 (25)

is the partition function in the case when the central site is chosen to be a spin-5/2 site. Thus, for given values of s_0 , the magnetization is obtained as

$$M_{5/2} = \frac{1}{2} \left[5 e^{\frac{\beta}{2}(25D_A/2+5h)} X_1^q - 5 e^{\frac{\beta}{2}(25D_A/2-5h)} X_2^q + 3 e^{\frac{\beta}{2}(9D_A/2+3h)} X_3^q - 3 e^{\frac{\beta}{2}(9D_A/2-3h)} X_4^q + e^{\frac{\beta}{2}(D_A/2+h)} X_5^q - e^{\frac{\beta}{2}(D_A/2-h)} \right] \times \left[e^{\frac{\beta}{2}(25D_A/2+5h)} X_1^q + e^{\frac{\beta}{2}(25D_A/2-5h)} X_2^q + e^{\frac{\beta}{2}(9D_A/2+3h)} X_3^q + e^{\frac{\beta}{2}(9D_A/2-3h)} X_4^q + e^{\frac{\beta}{2}(D_A/2+h)} X_5^q + e^{\frac{\beta}{2}(D_A/2-h)} \right]^{-1}.$$
 (26)

By analogy to all the calculations given above, the magnetization values for spin-3 sites may be obtained by picking the central site as spin-3 and repeating the whole procedure. However, we do not repeat them and just give the final result as follows

$$M_{3} = Z_{3}^{-1} \sum_{\{\sigma_{0}\}} \sigma_{0} P(\{\sigma_{0}\}) =$$

$$Z_{3}^{-1} \sum_{\{\sigma_{0}\}} \sigma_{0} e^{\beta(D_{B}\sigma_{0}^{2} + h\sigma_{0})} g_{m}^{q}(s_{0}), \qquad (27)$$

(20)

where
$$Z_{3} = \sum_{\{\sigma_{0}\}} e^{\beta(D_{B}\sigma_{0}^{2} + h\sigma_{0})} g_{m}^{q}(\sigma_{0})$$
(28)

is the partition function in the case the central site is picked to be a spin-3 site. Finally, the magnetization is given as

$$M_{3} = \left[3e^{\beta(9D_{B}+3h)}Y_{1}^{q} - 3e^{\beta(9D_{B}-3h)}Y_{2}^{q} + 2e^{\beta(4D_{B}+2h)}Y_{3}^{q} - 2e^{\beta(4B-2h)}Y_{4}^{q} + e^{\beta(D_{B}+h)}Y_{5}^{q} - e^{\beta(D_{B}-h)}Y_{6}^{q} \right] \times \left[e^{\beta(9D_{B}+3h)}Y_{1}^{q} + e^{\beta(9D_{B}-3h)}Y_{2}^{q} + e^{\beta(4D_{B}+2h)}Y_{3}^{q} + e^{\beta(4B-2h)}Y_{4}^{q} + e^{\beta(D_{B}+h)}Y_{5}^{q} + e^{\beta(D_{B}-h)}Y_{6}^{q} + 1 \right]^{-1}.$$
 (29)

Assuming that the bilinear interaction parameter J between spin-5/2 and spin-3 sites is of antiferromagnetic type, i.e., the nearest neighbors are aligned antiparallel to each other, the total magnetization is given as

$$M_T = \frac{1}{2} \left(M_{5/2} + M_3 \right), \tag{30}$$

which will help us to elucidate the compensation behaviors of our model.

3. Discussions of the numerical findings

3.1. Ground-state phase diagrams

The zero-temperature phase diagram, or ground state phase diagram, is crucial in the study of magnetic systems. To construct it, we used the internal energy per site, defined as

$$E_0 = s_i \sigma_j - \frac{1}{q|J|} \left(D_A s_i^2 + D_B \sigma_j^2 \right). \tag{31}$$

Considering the eigenvalues of type-s and type- σ , we determine all spin configurations and their corresponding energies (Table I). By identifying the values of D_A and D_B that minimize each configuration's energy, we constructed the ground state phase diagram in the $(D_A/q|J|,D_B/q|J|)$ planes for all q. As shown in Fig. 2, this phase diagram reveals eleven phase configurations, eight multiphase points, and several multiphase lines. Our results are qualitatively comparable to those of [38], despite the latter being based on a square lattice rather than a Bethe lattice.

3.2. Thermal behaviors of sublattice magnetizations

This section presents the thermal variations of the magnetizations $M_{5/2}$ and M_3 of the two sublattices, aiming to establish a correspondence between these

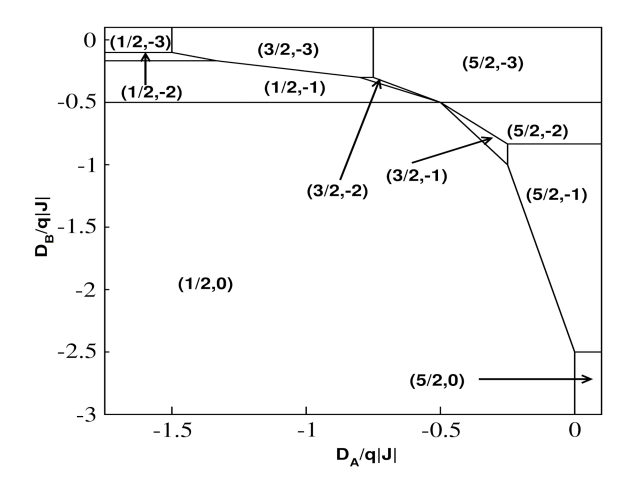


Fig. 2. Ground state phase diagram of the model in the $(D_A/q|J|, D_B/q|J|)$ plane. Here, q denotes the coordination number, i.e., the number of nearest neighbors.

TABLE I

Energies of the different spin configurations of the ground state phase diagram for the mixed spin-5/2 and spin-3.

Ground state	Energy
(5/2, -3)	$E_1 = \frac{15}{2} - \frac{1}{q J } \left(\frac{25}{4} D_A + 9D_B \right)$
(5/2, -2)	$E_2 = 5 - \frac{1}{q J } \left(\frac{25}{4} D_A + 4D_B \right)$
(5/2, -1)	$E_3 = \frac{5}{2} - \frac{1}{q J } \left(\frac{25}{4} D_A + D_B \right)$
(5/2,0)	$E_4 = -\frac{25}{4q J }D_A$
(3/2, -3)	$E_5 = \frac{9}{2} - \frac{1}{q J } (\frac{9}{4} D_A + 9D_B)$
(3/2, -2)	$E_6 = 5 - \frac{1}{q J } \left(\frac{25}{4} D_A + 4D_B \right)$
(3/2, -1)	$E_7 = \frac{3}{2} - \frac{1}{q J } (\frac{9}{4} D_A + 9D_B)$
(3/2,0)	$E_8 = -\frac{9}{4q J }D_A$
(1/2, -3)	$E_9 = \frac{3}{2} - \frac{1}{q J } (\frac{1}{4}D_A + 9D_B)$
(1/2, -2)	$E_{10} = 1 - \frac{1}{q J } (\frac{1}{4}D_A + 4D_B)$
(1/2, -1)	$E_{11} = \frac{1}{2} - \frac{1}{q J } (\frac{1}{4}D_A + D_B)$
(1/2, 0)	$E_{12} = -\frac{1}{4q J }D_A$

magnetizations and the various spin configurations predicted by the ground-state phase diagram analyzed in Sect. 3.1.

In Fig. 3, the thermal behaviors of the sublattice magnetizations $M_{5/2}$ and M_3 are presented for various values of crystal fields, D_A and D_B . It is evident that the anisotropy plays a crucial role in determining the spin configurations at kT/|J|=0. Specifically, for fixed values of $D_A/|J|$ with $D_B/|J|=0.25$ (Fig. 3a), the magnetization of sublattice B, i.e., M_3 , adopts a single saturation value $M_3=3.0$, while $M_{5/2}$ exhibits multiple saturation values, namely $\frac{1}{2}$, 1, $\frac{3}{2}$, 2, and $\frac{5}{2}$. Similarly,

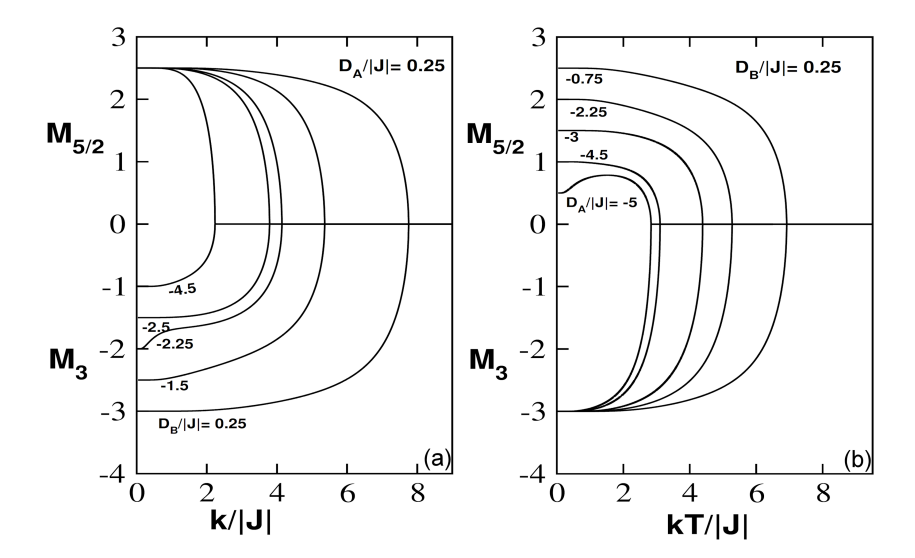


Fig. 3. Thermal behaviors of the sublattice magnetizations $M_{5/2}$ and M_3 for various values of crystal field interactions; (a) the curves displayed when $D_B/|J| = 0.25$ for selected values of $D_A/|J|$ and (b) the curves displayed with $D_A/|J| = 0.25$ for selected values of $D_B/|J|$.

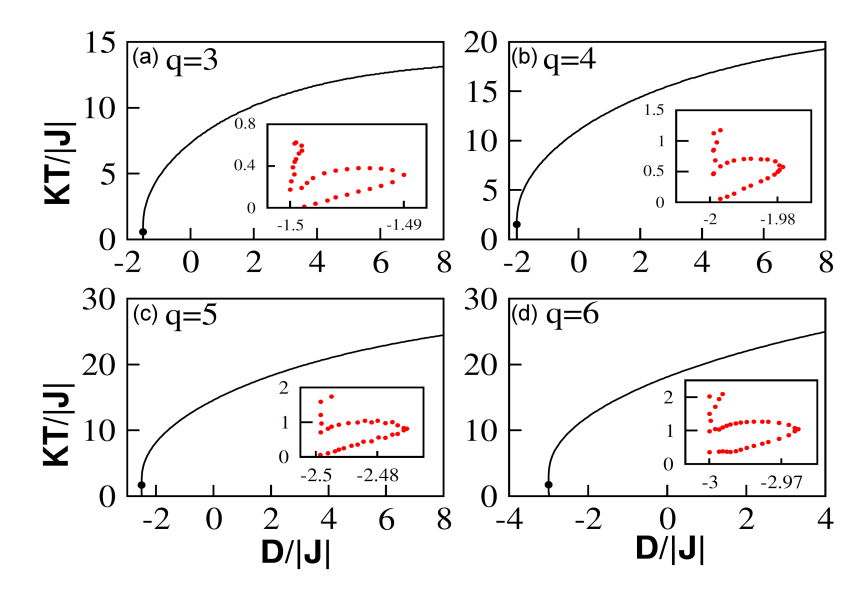


Fig. 4. Temperature-dependent phase diagrams in the $(D_B/|J|, kT/|J|)$ planes for q = 3, 4, 5, and 6. The solid and dashed lines refer to the second-order and the first-order phase transition lines, respectively. The dotted curves represent the compensation temperature lines. The solid circles refer to tricritical points.

for fixed values of $D_B/|J|$ with $D_A/|J|=0.25$ (Fig. 3b), the magnetization of sublattice A, i.e., $M_{5/2}$, takes a single saturation value $M_{5/2}=2.5$, while M_3 presents several saturation values, namely $1, \frac{3}{2}, 2, \frac{5}{2}$, and 3.

 $\bar{\Lambda}$ direct comparison with the ground-state phase diagram in Fig. 2 confirms a perfect agreement between the numerical results and the predicted configurations. Furthermore, in both cases, the absolute values of $|M_3|$ and $|M_{5/2}|$ decrease smoothly as temperature increases and eventually vanish at the critical temperature T_c . These findings align qualitatively with previous studies [23, 24], despite differences in spin values.

3.3. Phase diagrams and magnetic properties

The phase diagrams of this study are plotted in the $(D_A/|J|,kT)$ and $(D_B/|J|,kT)$ planes for given values of $D_B/|J|$ and $D_A/|J|$, respectively. They include the second-order transition lines (T_c) , first-order transition lines (T_t) creating the magnetizations discontinuities, and compensation lines $(T_{\rm comp})$ where sublattice magnetizations cancel out. The solid and dashed lines in the figures represent T_c and T_t , respectively, while the red dotted lines indicate $T_{\rm comp}$. The tricritical points, where the T_c -and T_t -lines merge, are marked by solid circles.

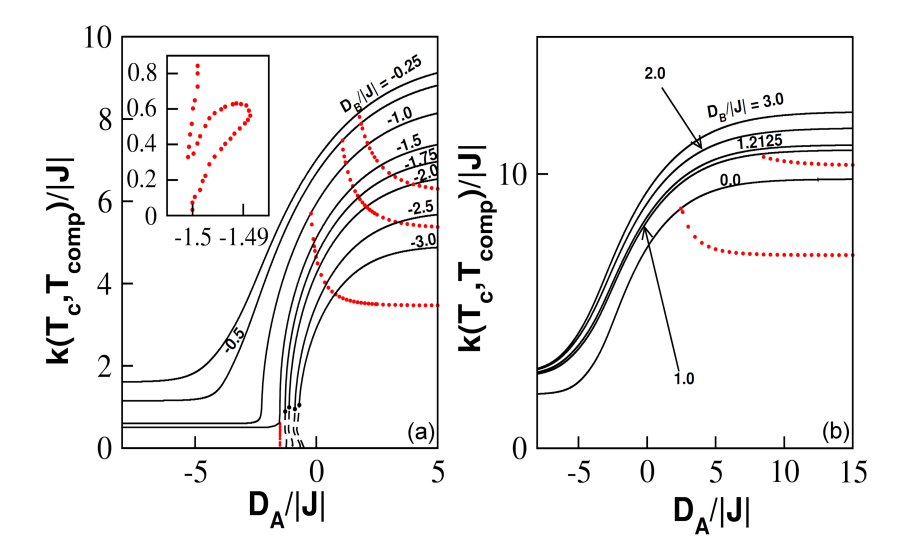


Fig. 5. Temperature-dependent phase diagrams in the $(D_A/|J|, kT/|J|)$ planes for given values of $D_B/|J|$, as indicated on the curves, when q=3. The solid and dashed lines refer to the second-order and the first-order phase transition lines, respectively. The dotted curves represent the compensation temperature lines. The solid circles refer to tricritical points.

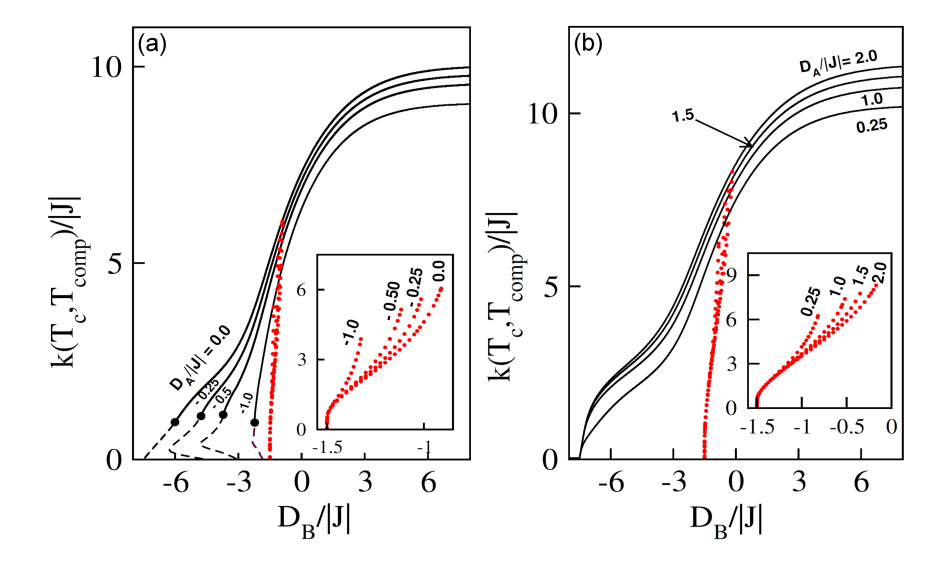


Fig. 6. Temperature-dependent phase diagrams in the $(D_B/|J|, kT/|J|)$ planes for given values of $D_A/|J|$, as indicated on the curves, with q=3. The solid and dashed lines refer to the second-order and the first-order phase transition lines, respectively. The dotted curves represent the compensation temperature lines. The solid circles refer to tricritical points.

The first phase diagrams are illustrated in the (D/|J|,kT/|J|) plane for $q=3,\,4,\,5,$ and 6 when $D=D_A=D_B,$ as shown in Fig. 4. The T_t -lines start at zero temperature for each q and from the values of $D=-\frac{q|J|}{2}$ connect to the corresponding T_c -lines at their tricritical points. The critical temperature increases with D and saturates beyond a threshold value of D for each q. The temperatures corresponding to these lines increase with increasing q, which is a well-known behavior. The compensation lines indicate multi-compensation behavior. Specifically, when $-\frac{q}{2} < D/|J| \le \alpha$, where $\alpha = -1.49875, -1.97842, -2.4704,$ and -2.9629 for

 $q=3,\ 4,\ 5,\ {\rm and}\ 6,\ {\rm respectively,\ two\ compensation\ points\ emerge.\ Near\ }D/|J|=-\frac{q}{2},\ {\rm up\ to\ four\ compensation\ points\ can\ appear.\ These\ different\ results\ confirm\ that\ the\ system\ presents\ tricritical\ and\ compensation\ phenomena\ for\ all\ q\ values.}$

The second phase diagrams (Fig. 5) are plotted in the $(D_A/|J|, kT)$ plane for different values of $D_B/|J|$ and q=3. For $D_B/|J|<-1.5$, i.e., for $D_B/|J|=-3.0$, -2.5, -2.0, -1.75 (Fig. 5a), the observed critical and tricritical behaviors are consistent with the trends in Fig. 4. Notably, no compensation behavior is observed for these values of $D_B/|J|$. For $D_B/|J| \ge -1.5$, only second-order

phase transitions occur. In this range, T_c -lines become nearly parallel to the $D_A/|J|$ -axis at extreme values of $D_A/|J|$. These lines originate at lower temperatures for negative values of $D_A/|J|$ and increase with $D_A/|J|$. Similarly, the transition temperatures corresponding to these lines increase with $D_B/|J|$. Compensation behavior appears for $-1.5 \leq D_B/|J| \leq 1.2125$, where a single compensation point is observed when $D_B/|J| > -1.5$. These lines emerge from their corresponding critical lines, decrease gradually, and become nearly linear as $D_A/|J|$ increases. For $D_B/|J| = -1.5$, multi-compensation behavior occurs, as highlighted in the inset in Fig. 5a. In particular, in the vicinity of $D_B/|J| = -1.5$, up to four compensation points can appear, indicating reentrant

The last phase diagrams (Fig. 6) plotted in the $(D_B/|J|, kT/|J|)$ plane are calculated for different $D_A/|J|$ values and q=3. As shown in Fig. 6a, for $D_A/|J| \leq 0.0$, the first-order phase transition lines originate at zero temperature from a specific value of $D_B/|J|$, then gradually increase and merge with their corresponding second-order transition line at tricritical points. This confirms tricritical behavior for all $D_A/|J| \le 0.0$. When $D_A/|J| > 0.0$ (Fig. 6b), the system exhibits only the second-order phase transitions. In this regime, the transition lines originate around $D_B/|J| = -7.48$ at zero temperature and increase with $D_B/|J|$. As observed in the insets, all the compensation lines originate from the same specific value of $D_B/|J| = -1.5$ at zero temperature for all $D_A/|J|$ values, increasing with $D_B/|J|$ and terminating near the critical line. The overall trends in Figs. 5 and 6 align with previous studies on mixed spin-(2, 5/2) systems [19, 22].

To further illustrate the system's critical, tricritical, and reentrant behaviors, the thermal variations of the sublattice magnetizations for selected parameter values are presented in Fig. 7a–d. The system transits from the disordered paramagnetic phase to an ordered phase before reentering the disordered paramagnetic phase, with first- or second-order transitions. These figures confirm the existence of critical, tricritical, and reentrant behaviors in the investigated system.

Finally, the total magnetization $|M_T|$ is examined to distinguish multi-compensation phenomena. As shown in Fig. 8a–d, one, two, three, or even four compensation points emerge for specific parameter values. These findings are in full agreement with the phase diagrams presented earlier.

3.4. Hysteresis properties analysis

In this section, we have systematically examined the hysteresis behavior of the system by analyzing the effects of key model parameters, namely the crystal field values and temperature.

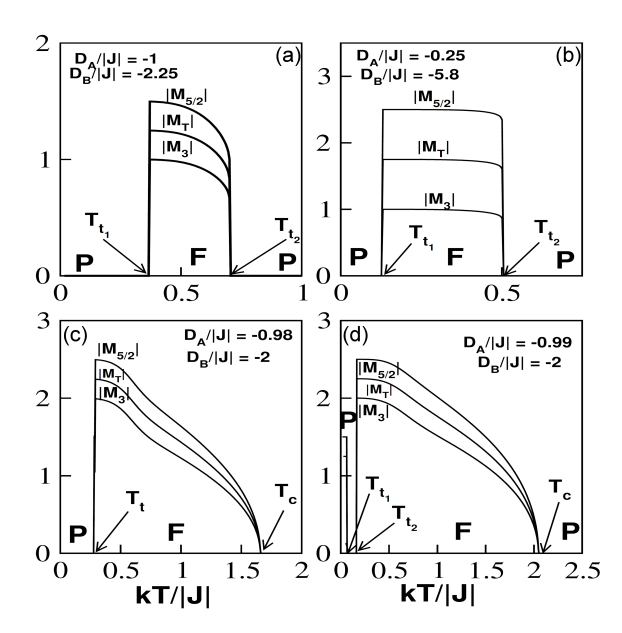


Fig. 7. Thermal behaviors of the sublattice magnetizations $|M_{5/2}|$, $|M_3|$ and total magnetization $|M_T|$ for several values of crystal fields $D_A/|J|$ and $D_B/|J|$, as indicated in different panels of the figure, with q=3. Here, T_t and T_c indicate first-order and second-order transition temperatures, respectively.

First, we investigate the influence of temperature on the hysteresis behavior while keeping one of the crystal fields fixed at a specific value and setting the others to zero, i.e., for $D_A/|J| = 0.0$ and $D_B/|J| = -1.2$, as shown in Fig. 9a–f. The result reveals a multi-hysteresis behavior characterized by a gradual reduction in the number of hysteresis loops as the temperature increases. For kT/|J| < 2.5 (Fig. 9a), the system exhibits three hysteresis loops — a central loop connected to two lateral loops. As temperature increases within the range of $2.5 \le kT/|J| < 5.0$ (Fig. 9b-d), the central loop vanishes, leaving only two narrow loops near zero magnetic field. A further temperature increase reduces the number of loops to one in the range of $5.0 \le kT/|J| < 5.6$ (Fig. 9e). Finally, at kT/|J| = 5.6 (see Fig. 9f), all hysteresis loops disappear as this temperature exceeds the critical temperature $kT_c/|J| \simeq 5.58$, beyond which the system transitions into the paramagnetic phase. By altering the action of the crystal fields on the sublattice sites, i.e., for $D_A/|J| = -1.2$ and $D_B/|J| = 0.0$ (Fig. 10a-f), similar hysteresis behaviors are observed. However, in this case, a single loop appears, whose size and width progressively decrease with increasing temperature before disappearing.

Next, we analyze the cases where one of the crystal fields, D_A or D_B , is fixed and the other varies. In Fig. 11a–f, we present the hysteresis loops of the total magnetization at the constant temperature kT/|J| = 0.5 and $D_A/|J| = -1.0$ for

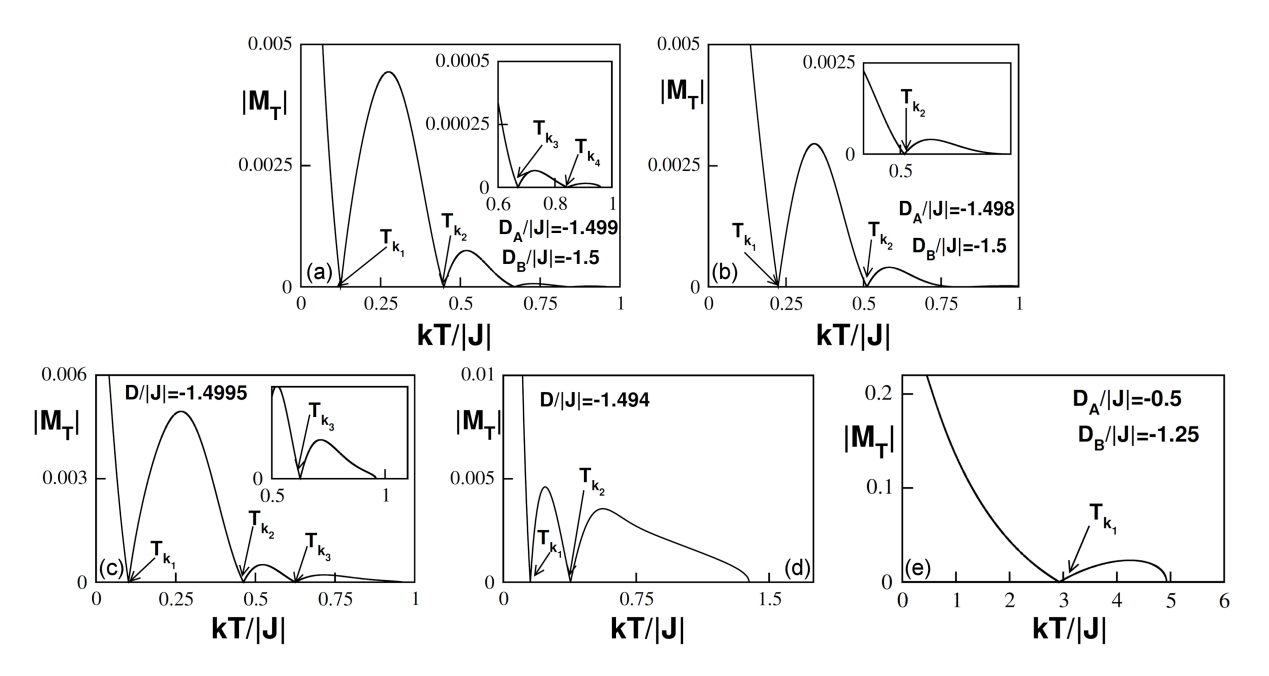


Fig. 8. Thermal behaviors of the total magnetization $|M_T|$ for various values of crystal fields $D_A/|J|$ and $D_B/|J|$ or $D/|J| = D_A/|J| = D_B/|J|$, as indicated in different panels, with q = 3. The model shows one, two, three, or four compensation temperatures indicated with T_k .

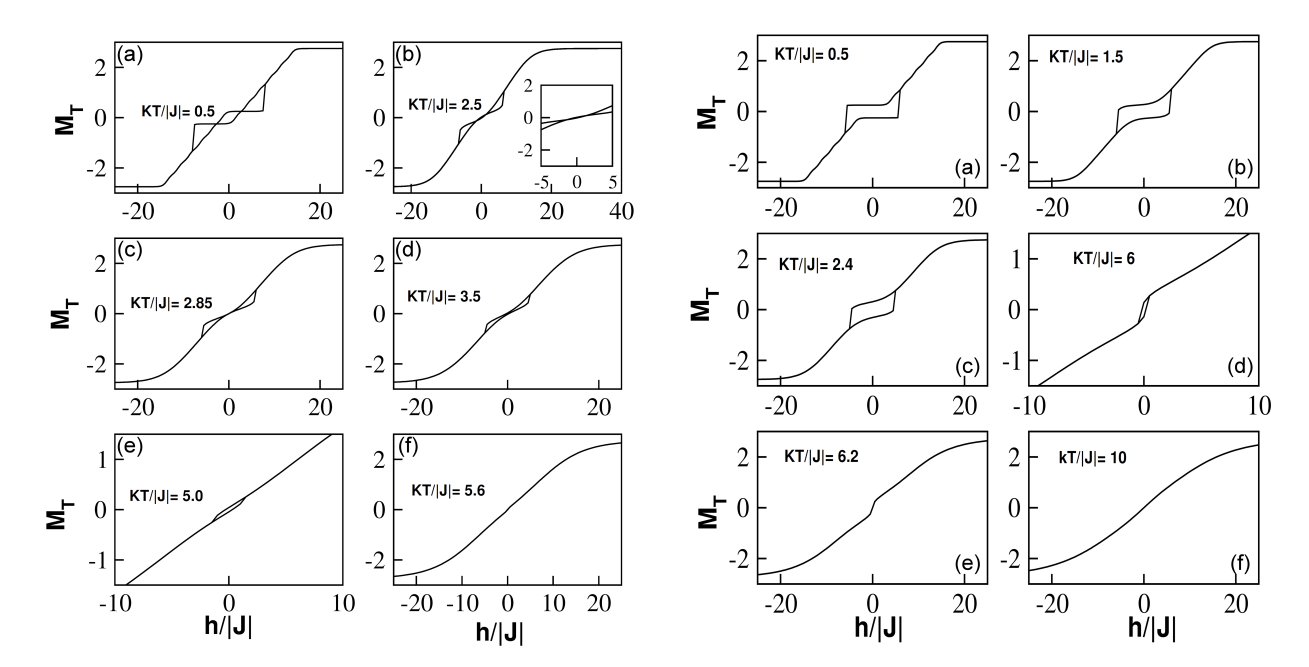


Fig. 9. Hysteresis properties of the model for $D_A/|J|=0.0$, $D_B/|J|=-1.2$, and given values of the temperature indicated in different panels of the figure.

Fig. 10. Hysteresis properties of the model for $D_A/|J| = -1.2$, $D_B/|J| = 0.0$, and given values of the temperature indicated in different panels of the figure.

different values of $D_B/|J|$. When $D_B/|J| > -0.3$, a single hysteresis loop is observed (Fig. 11a). However, for $D_B/|J| \leq -0.3$, a multi-hysteresis behavior emerges; the number of hysteresis loops changes from three to two and then to one before disappearing as the system enters the paramagnetic phase (Fig. 11b-f). In Fig. 12a-f, plotted

for $D_B/|J|=-1.0$ and selected values of $D_A/|J|$, the observed hysteresis behaviors differ from those in Fig. 11. Specifically, a multi-hysteresis behavior with three loops appears when $D_A/|J| \geq -1.0$ (Fig. 12a-b), while for $D_A/|J| < -1.0$, a single loop is observed, whose size and width gradually decrease (Fig. 12c-f).

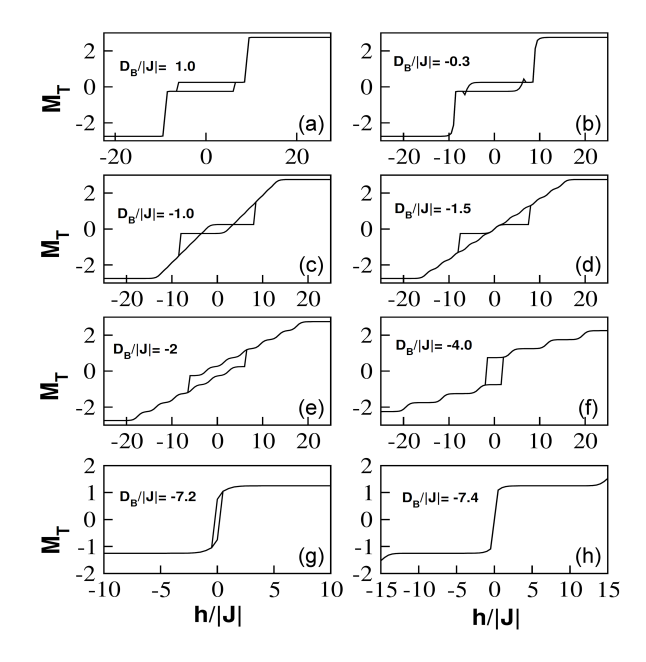


Fig. 11. Hysteresis properties of the model for kT/|J| = 0.5, $D_A/|J| = -1$, and given values of $D_B/|J|$ indicated in different panels of the figure.

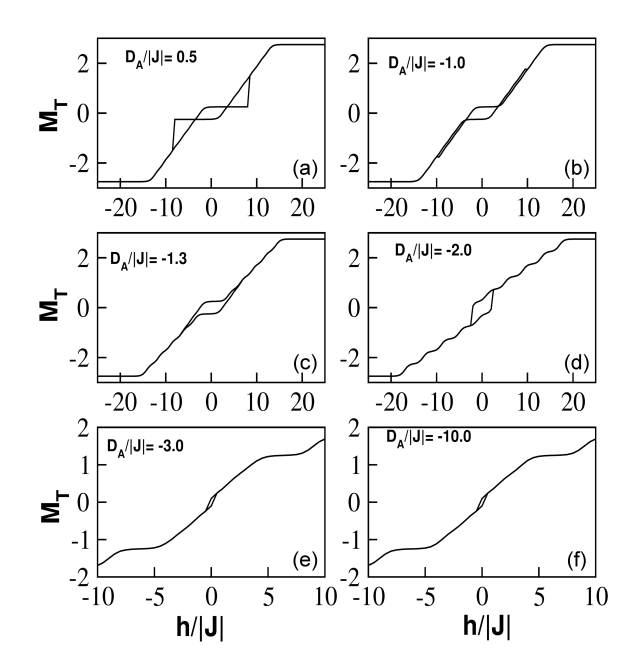


Fig. 12. Hysteresis properties of the model for kT/|J| = 0.5, $D_B/|J| = -1$, and given values of $D_A/|J|$ indicated in different panels of the figure.

Finally, we investigate the influence of a uniform crystal field on the hysteresis behavior at a fixed temperature value kT/|J|=2.0 (Fig. 13a–f). As shown in the figure, the uniform crystal field significantly impacts the hysteresis behavior — when D/|J|>-0.5, a single hysteresis loop is observed, whereas for $-1 \le D/|J| \le -0.5$, three loops appear. For D/|J|<-1.0, the system reverts to a single hysteresis loop before it vanishes as D/|J|

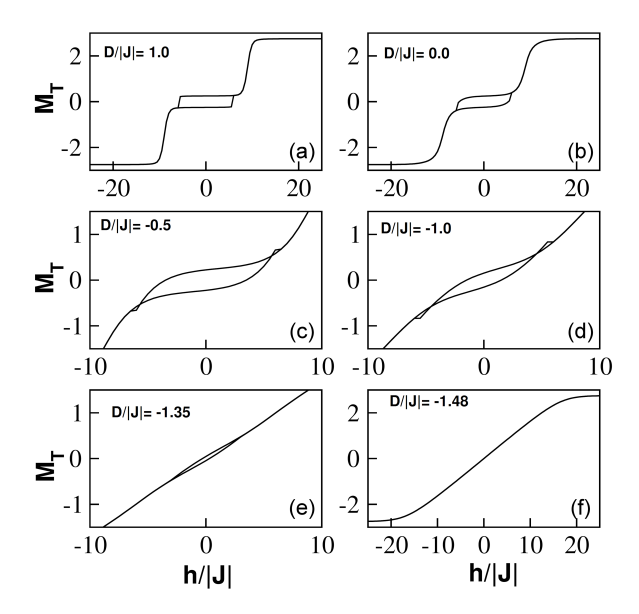


Fig. 13. Hysteresis properties of the model for kT/|J| = 2.0 and given values of D/|J| indicated in different panels of the figure.

decreases further. The hysteresis behavior observed in our model is consistent with previous findings reported in [19].

4. Conclusions

In this investigation, we employed the exact recursion relations approach to study the magnetic properties of a mixed spin-5/2 and spin-3 ferrimagnetic Ising system on the Bethe lattice. Our comprehensive analysis of thermal variations of magnetizations and phase transitions has led to the construction of complex magnetic phase diagrams. The key phenomena identified include first- and second-order phase transitions, tricritical points, multiple compensation points, and reentrant behavior.

Furthermore, we examined the system's response to an external magnetic field, revealing complex hysteresis phenomena, including multi-loop hysteresis cycles. Our findings are in perfect agreement with existing literature, particularly with [22], which studied a similar spin model with spin-5/2 and spin-2 on a square lattice using the meanfield approximation. However, our study differs from [37, 38] in two significant ways: (i) the use of Bethe lattice, in contrast to the lattice structures considered in those works, and (ii) the adoption of an exact recursive approach, which allows for a more detailed exploration of additional system features, such as the observed multi-compensation behavior.

To further advance this study, we intend to explore the impact of next-nearest-neighbor interactions on the magnetic properties revealed herein. This investigation will be conducted using both

the recursion relations method and Monte Carlo simulations, the latter being among the most reliable techniques for analyzing complex magnetic systems.

References

- [1] F.P. Montiel, N. De La Espriella, J.C. Madera, J. Phys. Conf. Ser. **2046**, 012013 (2021).
- [2] M. Karimou, G.D. Ngantso, C.M. Salgado, A.S. de Arruda, *Chin. J. Phys.* 88, 879 (2024).
- [3] T. Bahlagui, A. El Kenz, A. Benyoussef, J. Supercond. Nov. Magn. 31, 4179 (2018).
- [4] M. Karimou, N. De La Espriella, *Physica A* 531, 121738 (2019).
- [5] M. Karimou, R.A. Yessoufou, G. Dimitri Ngantso, F. Hontinfinde, E. Albayrak, *Condens. Matter Phys.* 22, 33601 (2019).
- [6] J.S. da Cruz Filho, M. Godoy, A.S. de Arruda, *Physica A* 392, 6247 (2013).
- [7] Y. Guo, G. F. Xu, C. Wang, T.T. Cao, J. Tang, Z.Q. Liu, Y. Ma, S.P. Yan, P. Cheng, D.Z. Liao, *Dalton Trans.* 41, 1624 (2012).
- [8] S.M. Holmes, G.S. Girolami, J. Am. Chem. Soc. 121, 5593 (1999).
- [9] H. Svendsen, J. Overgaard, M. Chevalier, E. Collet, Y.S. Chen, F. Jensen, B.B. Iversen, *Chemistry* 16, 7215 (2010).
- [10] Y.Z. Zhang, G.P. Duan, O. Sato, S. Gao, J. Mater. Chem. 16, 2625 (2006).
- [11] S. Ohkoshi, K.I. Arai, Y. Sato, K. Hashimoto, Nat. Mater. 3, 857 (2004).
- [12] A. Dakhama, N. Benayad, J. Magn. Magn. Mater. 213, 117 (2000).
- [13] G.M. Buendia, M.A. Novotny, *J. Phys. Condens. Matter* **9**, 5951 (1997).
- [14] A. Zaim, M. Kerouad, Physica A 389, 3435 (2010).
- [15] A. Bobák, O.F. Abubrig, D. Horváth, J. Magn. Magn. Mater. 246, 177 (2002).
- [16] W.G. Zhu, M.H. Ling, Commun. Theor. Phys. **51**, 756 (2009).

- [17] B. Deviren, Y. Polat, M. Keskin, *Chin. Phys. B* 20, 060507 (2011).
- [18] A. Feraoun, S. Amraoui, M. Kerouad, Physica A 526, 120924 (2019).
- [19] W. Wei, D. Lv, F. Zhang, J.L. Bi, J.N. Chen, J. Magn. Magn. Mater. 385, 16 (2015).
- [20] N. De La Espriella, C.A. Mercado, J.C. Madera, J. Magn. Magn. Mater. 401, 22 (2016).
- [21] H. Bouda, L. Bahmad, R. Masrour, A. Benyoussef, J. Supercond. Nov. Magn. 32, 1837 (2019).
- [22] J.S. da Cruz Filho, T.M. Tunes, M. Godoy, A.S. de Arruda, *Physica A* 450, 180 (2016).
- [23] A.A. Arabi, H.K. Mohamad, *AIP Conf. Proc.* **2398**, 020070 (2022).
- [24] A.A. Arabi, H.K. Mohamad, *Solid State Commun.* **338**, 114456 (2021).
- [25] E. Albayrak, M. Keskin, J. Magn. Magn. Mater. 261, 196 (2003).
- [26] E. Albayrak, Int. J. Mod. Phys. B 17, 1087 (2003).
- [27] E. Albayrak, A. Alçi, *Physica A* **345**, 48 (2005).
- [28] E. Albayrak, A. Yigit, *Physica A* **349**, 471 (2005).
- [29] E. Albayrak, A. Yigit, *Phys. Status Solidi* (b) **242**, 1510 (2005).
- [30] E. Albayrak, *Physica A* **375**, 174 (2007).
- [31] E. Albayrak, *Physica B* **391**, 47 (2007).
- [32] E. Albayrak, Mod. Phys. Lett. B 32, 1850177 (2018).
- [33] E. Albayrak, A. Yigit, *Phys. Lett. A* **353**, 121 (2006).
- [34] R.A. Yessoufou, S.H. Amoussa, F. Hontinfinde, *Cent. Eur. J. Phys.* **7**, 555 (2009).
- [35] R. Gupta, M. Kumar, *Mater. Sci. Eng. B* **178**, 195 (2013).
- [36] P. Gütlich, A. Hauser, H. Spiering, *Chem. Rev.* 114, 991 (2014).
- [37] I.A. Obaid, H.K. Mohamad, S.D. Al-Saeedi, *Ukr. J. Phys.* **67**, 695 (2022).
- [38] I.A. Obaid, S.D. Al-Saeedi, H.K. Mohamad, *Univ. Thi-Qar J. Sci.* **10**, 145 (2023).